

# Dalton Transactions

Accepted Manuscript



This is an *Accepted Manuscript*, which has been through the Royal Society of Chemistry peer review process and has been accepted for publication.

*Accepted Manuscripts* are published online shortly after acceptance, before technical editing, formatting and proof reading. Using this free service, authors can make their results available to the community, in citable form, before we publish the edited article. We will replace this *Accepted Manuscript* with the edited and formatted *Advance Article* as soon as it is available.

You can find more information about *Accepted Manuscripts* in the [Information for Authors](#).

Please note that technical editing may introduce minor changes to the text and/or graphics, which may alter content. The journal's standard [Terms & Conditions](#) and the [Ethical guidelines](#) still apply. In no event shall the Royal Society of Chemistry be held responsible for any errors or omissions in this *Accepted Manuscript* or any consequences arising from the use of any information it contains.

## ARTICLE

# Solid-State Emission Enhancement in Vaulted *trans*-Bis(salicylaldiminato)platinum(II) Crystals with Halogen Functionality<sup>†</sup>

Cite this: DOI: 10.1039/x0xx00000x

Received 00th January 2012,  
Accepted 00th January 2012

DOI: 10.1039/x0xx00000x

www.rsc.org/

Naruyoshi Komiya, Minoru Okada, Kanako Fukumoto, Shotaro Iwata and Takeshi Naota\*

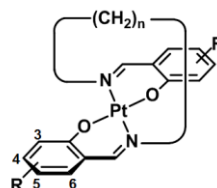
The synthesis, structure, and solid-state emission of vaulted *trans*-bis(salicylaldiminato)platinum(II) complexes **1–3** with halogen functionalities are described and compared with the non-substituted analogues. Chloro-substitution provided an improvement of the low emission properties of short-vaulted, non-substituted complexes **1** and **2** in the crystalline state at ambient temperature, while the intense emission of long-vaulted analogues **3** remained unchanged. Bromo-substituted crystals also emit intensively, while the fluoro analogue is non-emissive under the same conditions. Temperature-dependent emission spectra indicate that all chloro- and bromo-substituted crystals with enhanced emission properties at ambient temperature exhibit improved heat resistance properties towards emission decay with the halogen functionalities. X-ray diffraction studies revealed that such the positive effect of halogenation for the enhancement of solid-state emission is due to significant molecular constraint in the crystals by a combination of the vaulted structure and three dimensional H $\cdots$ X hydrogen bonding interactions.

## Introduction

Studies on the solid-state emission of transition-metal complexes is important for the development of new functional materials that exhibit various stimuli-responsive emission properties, such as electroluminescence,<sup>1</sup> vapochromism,<sup>2</sup> and mechanochromism.<sup>3</sup> Phosphorescent crystals of transition-metal complexes are extensively studied,<sup>2,3</sup> due to their potential for high-density integration, with the aim to realize intense solid-state emission, although the emission of transition-metal complexes in the crystalline state is typically weaker than that in the solution state, due to the negative intermolecular effects in d- $\pi$  conjugation systems.<sup>4</sup> Two contrasting strategies have been employed in molecular and crystal design to enhance the solid-state emission of transition-metal complex crystals; the functionalization of bulky groups on each phosphor unit to avoid significant molecular contacts such as  $\pi$ - $\pi$  stacking<sup>5,6</sup> and the construction of metal-metal interactions.<sup>2,3,5–8</sup>

Recently, we have investigated the correlation between solid-state emission and the molecular array of polymethylene- and polyoxyethylene-vaulted *trans*-bis(salicylaldiminato)platinum(II) complexes in the crystalline state,<sup>5a,b</sup> where the specific heat resistance towards emission decay with increasing temperature was found to be essential for intense phosphorescence at ambient temperature. Single-crystal X-ray diffraction (XRD) studies strongly suggest that higher-ordered molecular constraint by intermolecular interactions is an

important factor for solid-state emission and the heat resistance properties of the crystals. To gain further insight into the intermolecular factors for the enhancement of solid-state emission, the effect of halogen functionalization of polymethylene-vaulted *trans*-bis(salicylaldiminato)platinum(II) complexes **1–3** ( $n = 10–12$ ) was investigated. The introduction of chloro- and bromo-substituents to the aromatic rings of vaulted platinum complexes enhance the emission properties in the crystalline state by decreasing the structural dependence of the heat resistance properties,<sup>5a,b</sup> while the fluoro analogues are entirely non-emissive. The XRD results revealed that the present enhancement of emission by halogen functionalization is due to an increase in the dimensionality of the molecular constraint in the crystal units by a synergistic effect of the vaulted structure and the hydrogen bonding network with chlorine/bromine atoms.<sup>9</sup> The platform also exhibits a wide chromogenic change over 41 nm for solid-state emission, simply by chloro-substitution at different positions on the aromatic rings. Here, we describe the synthesis, structure, and solid-state emission of a series of polymethylene-vaulted *trans*-bis(salicylaldiminato)platinum(II) complex crystals bearing halogen functionalities, with a focus on the mechanistic rationale for the heat resistance properties based on the molecular arrays of the crystal unit.



- |             |         |
|-------------|---------|
| 1: $n = 10$ | a: 3-Cl |
| 2: $n = 11$ | b: 4-Cl |
| 3: $n = 12$ | c: 5-Cl |
|             | d: 6-Cl |
|             | e: 4-F  |
|             | f: 4-Br |
|             | g: H    |

## Results and discussion

### Synthesis and structure of vaulted complexes

A series of *trans*-bis(salicylaldiminato)platinum(II) complexes bearing polymethylene bridges with and without a halogen functionality **1–3** [**1**:  $n = 10$ ; **2**:  $n = 11$ ; **3**:  $n = 12$ ; **a**: 3-Cl (*ortho*-position of the phenol moiety); **b**: 4-Cl (*meta*-position); **c**: 5-Cl (*para*-position); **d**: 6-Cl (*ortho*-position of the imine moiety); **e**: 4-F; **f**: 4-Br; **g**: H] was prepared by reaction of  $\text{PtCl}_2(\text{CH}_3\text{CN})_2$  with the corresponding *N,N'*-bis(salicylidene)-1, $\omega$ -alkanediamines in boiling dimethyl sulfoxide (DMSO) and toluene. Non-vaulted, 4,4'-dichloro-*N,N'*-dimethyl complex **4b** was similarly prepared from *N*-(4-chlorosalicylidene)-methylamine. Racemic crystals employed for single-crystal XRD studies were obtained by recrystallization from EtOH. The *trans*-coordination and vaulted structures of **2b** and **3b–f** have been unequivocally established by single-crystal XRD at 113 K (Table 1). ORTEP<sup>10</sup> drawings of these crystals are

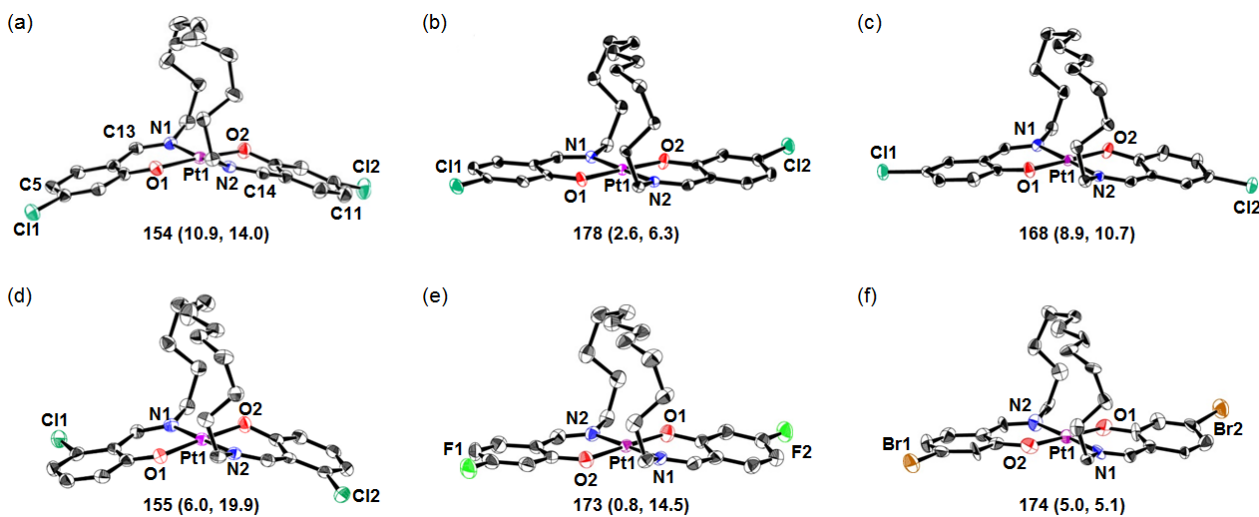


**Fig. 1** ORTEP representation of halo-substituted *trans*-bis(salicylaldiminato)platinum (a) (*S*)-**2b**, (b) (*S*)-**3b**, (c) (*S*)-**3c**, (d) (*S*)-**3d**, (e) (*S*)-**3e** and (f) (*S*)-**3f** as their racemic crystals. Thermal ellipsoids are shown at the 50% probability level. The angle of C(5)–Pt(1)–C(11) and dihedral angles of C(13)–N(1)–Pt(1)–O(1)/C(14)–N(2)–Pt(1)–O(2) (in parentheses) are given under each structure.

### Effect of halogen substituents on the emission properties in the crystalline state

Complexes **1–3** bearing chloro- and bromo-substituents on the aromatic rings generally exhibit intense solid state emission properties in the crystalline state under excitation at 420 nm, although  $2 \times 10^{-4}$  M solutions of these complexes in 2-methyltetrahydrofuran (2-MeTHF) are non-emissive at 298 K under the same conditions ( $\Phi_{298\text{K}} < 0.01$ ).<sup>5,7</sup> Crystals employed for photophysical analyses were obtained by recrystallization from EtOH for **1–3** and EtOAc for non-vaulted analogue **4b**. Photophysical data of **1–3** and **4b** in the crystalline state and in 2-MeTHF are given in Table 2 and Table S1, Supporting Information, respectively. Quantum efficiencies ( $\Phi$ ) were determined using the absolute method with an integrating sphere accessory.<sup>11</sup> The lifetimes ( $\tau$ ) of the crystals indicate that their emissions are phosphorescent.

shown in Fig. 1, where the angles of C(5)–Pt(1)–C(11) and dihedral angles of C(13)–N(1)–Pt(1)–O(1)/C(14)–N(2)–Pt(1)–O(2) are listed to express a macroscopic view of the coordination planarity for the *trans*-bis(salicylaldiminato)platinum moieties. The C(5)–Pt(1)–C(11) angles in short-bridged **2b** (unit 1: 154°; unit 2: 155°) are significantly smaller than those in long-bridged **3b** (178°; 179°), **3c** (168°), **3d** (155°), **3e** (173°), **3f** (174°; 178°), and the dihedral angles of C(13)–N(1)–Pt(1)–O(1)/C(14)–N(2)–Pt(1)–O(2) in **2b** (unit 1: 10.9°, 14.0°; unit 2: 10.2°, 18.5°) are much larger than those in **3b** (2.6°, 6.3°; 0.4°, 6.5°), **3c** (8.9°, 10.7°), **3d** (6.0°, 19.9°), **3e** (0.8°, 14.5°) and **3f** (5.0°, 5.1°; 0.3°, 9.2°). A correlation between the coordination planarity and the chain length in 4-Cl crystals **2b** and **3b** was also observed in the non-substituted complexes, as indicated in the C(5)–Pt(1)–C(11) angles of 162° for **1g**, 172° for **2g**, and 174° for **3g**.<sup>5b</sup> The specific bent structure of **3d** is due to stabilization by intermolecular stacking interactions as shown in Fig. 14b, discussed in the following section.

Crystal **3b** bearing 4-Cl and a dodecamethylene bridge exhibits intense yellow emission at 298 K under excitation at 420 nm ( $\Phi_{298\text{K}} = 0.29$ ), while non-vaulted, 4-Cl analogue **4b** emits very weak red-orange phosphorescence under the same conditions ( $\Phi_{298\text{K}} = 0.01$ ). The ratio of quantum efficiencies at 298 and 77 K ( $\Phi_{298\text{K}}/\Phi_{77\text{K}}$ ) is 0.71 for **3b** and 0.08 for **4b**, which indicates that vaulted **3b** has high heat resistance towards emission decay with increasing temperature, and non-vaulted **4b** is heat quenchable. The contrasting temperature-dependent emission profiles for **3b** and **4b** in the range of 77–298 K are shown in Fig. 2. The positive effect of vaulting on 4-chloro complexes is much greater than that on non-substituted analogues, as shown by the heat resistance properties ( $\Phi_{298\text{K}}/\Phi_{77\text{K}}$ ) of non-substituted, vaulted complex **3g** (0.63) and non-vaulted analogue **4g** (0.39).<sup>5a,b</sup> Figure 3 shows normalised emission spectra for **3b**, **4b**, **3g** and **4g** crystals at 298 K. Note that the emission maxima of the **4b** crystal ( $\lambda_{\text{max}} = 594$  nm) are

**Table 1** Crystallographic data for **2b**, **3b**, **3c**, **3d**, **3e** and **3f**

	(±)- <b>2b</b>	(±)- <b>3b</b>	(±)- <b>3c</b>	(±)- <b>3d</b>	(±)- <b>3e</b>	(±)- <b>3f</b>
formula	C <sub>25</sub> H <sub>30</sub> Cl <sub>2</sub> N <sub>2</sub> O <sub>2</sub> Pt	C <sub>26</sub> H <sub>32</sub> Cl <sub>2</sub> N <sub>2</sub> O <sub>2</sub> Pt	C <sub>26</sub> H <sub>32</sub> Cl <sub>2</sub> N <sub>2</sub> O <sub>2</sub> Pt	C <sub>26</sub> H <sub>32</sub> Cl <sub>2</sub> N <sub>2</sub> O <sub>2</sub> Pt	C <sub>26</sub> H <sub>32</sub> F <sub>2</sub> N <sub>2</sub> O <sub>2</sub> Pt	C <sub>26</sub> H <sub>32</sub> Br <sub>2</sub> N <sub>2</sub> O <sub>2</sub> Pt
<i>M<sub>r</sub></i>	656.52	670.55	670.55	670.55	637.64	759.45
<i>T</i> /K	113	113	113	113	113	113
crystal colour, habit	yellow, platelet	orange, block	orange, block	orange, block	yellow, block	yellow, block
crystal size/mm	0.30×0.20×0.10	0.30×0.30×0.20	0.50×0.40×0.30	0.60×0.20×0.20	0.40×0.30×0.30	0.10×0.06×0.06
crystal system	orthorhombic	triclinic	monoclinic	monoclinic	monoclinic	triclinic
space group	<i>Pbca</i> (#61)	<i>P</i> -1 (#2)	<i>P2</i> <sub>1</sub> / <i>c</i> (#14)	<i>P2</i> <sub>1</sub> / <i>c</i> (#14)	<i>C2</i> / <i>c</i> (#15)	<i>P</i> -1 (#2)
<i>a</i> /Å	14.0659(3)	10.5711(5)	18.462(1)	10.5969(5)	23.8726(8)	10.6479(8)
<i>b</i> /Å	24.2531(5)	11.6286(6)	11.4626(6)	10.0106(5)	10.2735(4)	11.7560(9)
<i>c</i> /Å	28.6200(7)	20.5715(10)	12.2654(6)	24.093(1)	20.2881(6)	20.876(2)
<i>α</i> /°	90	87.5780(10)	90	90	90	92.207(2)
<i>β</i> /°	90	87.8350(19)	99.383(1)	100.154(2)	98.850(1)	93.481(2)
<i>γ</i> /°	90	84.4990(18)	90	90	90	98.670(2)
<i>V</i> /Å <sup>3</sup>	9763.4(3)	2513.5(2)	2560.9(3)	2515.8(2)	4916.5(3)	2575.5(4)
<i>Z</i>	16	4	4	4	8	4
<i>ρ</i> <sub>calcd</sub> /gcm <sup>-3</sup>	1.786	1.772	1.739	1.770	1.723	1.958
<i>μ</i> (MoKα)/cm <sup>-1</sup>	59.691	57.987	56.914	57.933	57.254	85.642
<i>F</i> (000)	5152.00	1320.00	1320.00	1320.00	2512.00	1464.00
2 <i>θ</i> <sub>max</sub> /deg	55.0	54.9	55.0	54.9	54.9	55.0
no. of reflns measd	192498	49919	49653	48829	47837	51925
no. of obsd reflns	11136	11434	5843	5723	5609	11709
no. variables	557	595	298	298	298	595
<i>R</i> <sub>1</sub> ( <i>I</i> > 2σ( <i>I</i> )) <sup>a</sup>	0.039	0.022	0.044	0.039	0.027	0.069
<i>wR</i> <sub>2</sub> (all reflns) <sup>b</sup>	0.099	0.055	0.117	0.106	0.060	0.18
goodness of fit	1.05	1.09	1.13	1.07	1.07	1.09

<sup>a</sup> *R*<sub>1</sub> = Σ(|*F*<sub>o</sub>| - |*F*<sub>c</sub>|) / Σ(|*F*<sub>o</sub>|). <sup>b</sup> *wR*<sub>2</sub> = [Σ(*w*(*F*<sub>o</sub><sup>2</sup> - *F*<sub>c</sub><sup>2</sup>)<sup>2</sup>) / Σ *w*(*F*<sub>o</sub><sup>2</sup>)<sup>2</sup>]<sup>1/2</sup>.

**Table 2** Photophysical data for **1-4** in the crystalline state<sup>a</sup>

complex	<i>λ</i> <sub>abs</sub> (nm)	<i>λ</i> <sub>em</sub> (nm)	<i>Φ</i> <sup>b</sup>	<i>τ</i> (μs) <sup>c</sup>	CIE (x,y)
<b>1b</b> <sup>d</sup>	325, 436, 511	572	0.05 (0.35)	0.06	0.49, 0.50
<b>2b</b> <sup>d</sup>	321, 433, 509	580	0.12 (0.30)	1.36	0.52, 0.48
<b>3a</b> <sup>d</sup>	326, 444, 515	570	0.01 (0.24)	0.11	0.49, 0.51
<b>3b</b> <sup>d</sup>	327, 447, 511	544, 569	0.29 (0.41)	1.01	0.46, 0.54
<b>3c</b> <sup>d</sup>	333, 464, 535	598	0.10 (0.36)	0.74	0.56, 0.44
<b>3d</b> <sup>d</sup>	324, 458, 538	605	0.08 (0.17)	0.51	0.62, 0.38
<b>3e</b> <sup>d</sup>	305, 424, 500	— <sup>e</sup>	— <sup>e</sup> (0.49)	— <sup>e</sup>	— <sup>e</sup>
<b>3f</b> <sup>d</sup>	326, 440, 511	541, 568	0.20 (0.47)	0.60	0.46, 0.53
<b>4b</b>	326, 420, 504	594	0.01 (0.12)	0.08	0.55, 0.44

<sup>a</sup>Data obtained at 298 K under excitation at 420 nm. All crystals were obtained by recrystallization from EtOH or AcOEt. <sup>b</sup>Determined by the absolute method using an integrating sphere. <sup>c</sup>Values in parentheses are those measured at 77 K. <sup>d</sup>*λ*<sub>ex</sub> = 415 nm. <sup>e</sup>Racemic crystal. <sup>f</sup>No emission.

significantly red-shifted with respect to those of the **3b** crystal (544 nm) (Fig. 3a), while the emission spectra of the **3g** crystal is very similar to that of the **4g** crystal (Fig. 3b).<sup>5a,b</sup>

Dependence of the emission intensities on the linker length of 4-Cl-substituted crystals **1b–3b** is significantly different from those of non-substituted crystals **1g–3g**. Figure 4 shows the correlation between chain length and quantum efficiency for the **1–3** crystals. Although all crystals have significantly high quantum efficiencies at 77 K (*Φ*<sub>77K</sub> = 0.17–0.49, Fig. 4a), a clear chain-length dependence is observed at 298 K (Fig. 4b). Chloro-substituted crystals **1b–3b** emit weakly [*Φ*<sub>298K</sub> = 0.05 for **1b** (*n* = 10)], moderately [0.12 for **2b** (*n* = 11)] and more intensively [0.29 for **3b** (*n* = 12)] at 298 K as the chain lengths of the polymethylene bridges increase. In contrast, only the **3g** crystal exhibits a significant emission at 298 K (*Φ*<sub>298K</sub> = 0.32) among the non-substituted crystals, while the **1g** and **2g** analogues with shorter linkers are almost non-emissive under the same conditions (<0.01).<sup>5a,b</sup> The *Φ*<sub>298K</sub>/*Φ*<sub>77K</sub> ratios for Cl-substituted crystals **1b–3b** are higher (**1b**: 0.14; **2b**: 0.40; **3b**: 0.71) than those of non-substituted crystals **1g–3g** (**1g**: <0.01;

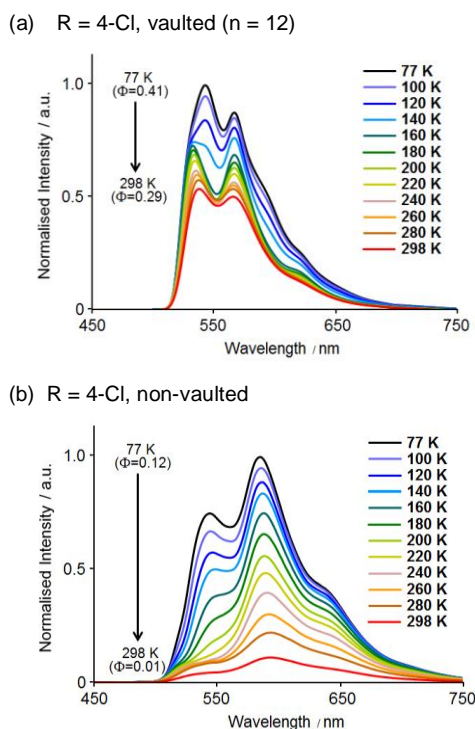


**Fig. 2** Temperature-dependence of emissions for (a) heat resistant **3b** and (b) heat quenchable **4b** crystals at 77 K–298 K ( $\lambda_{\text{ex}} = 420$  nm).

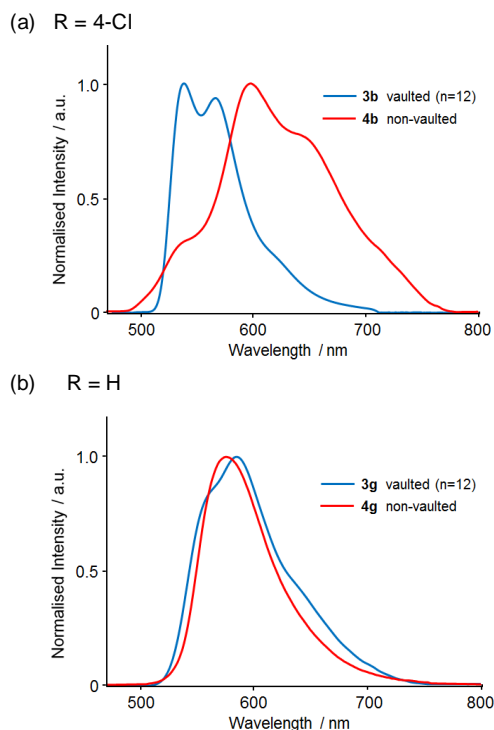


**Fig. 3** Normalised emission spectra for (a) 4-chloro crystals, **3b**, **4b** and (b) non-substituted crystals, **3g**, **4g** at 298 K ( $\lambda_{\text{ex}} = 420$  nm).

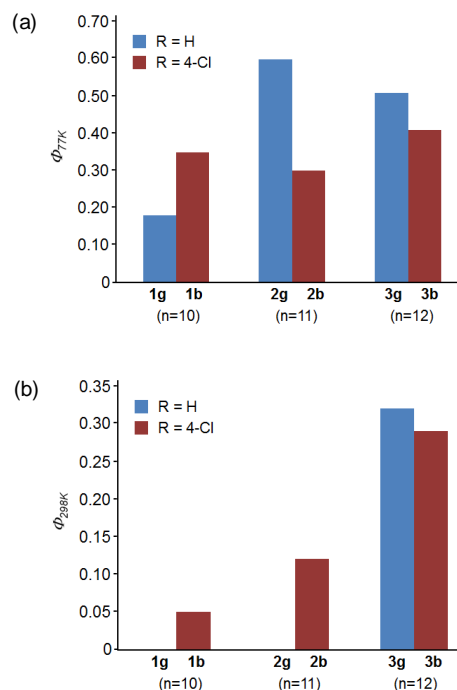


**Fig. 4** Correlation between chain length and quantum efficiency of **1–3** crystals at (a) 77 and (b) 298 K ( $\lambda_{\text{ex}} = 420$  nm).

**2g**: <0.01; **3g**: 0.63), which indicates that the original heat resistance properties of **1g–3g** crystals towards emission decay increases by substitution with the 4-Cl group on the aromatic rings. In addition, the extraordinarily high linker dependence of the heat resistance properties for the **1g–3g** crystals decreases significantly with halogen functionalization. Such contrasting linker-dependence of the heat resistance of chloro- and non-substituted crystals can be visualized by the temperature dependence of the emission spectra from 77 to 298 K, as shown in Fig. 5.

The strong halogen effect on the heat resistance properties of the vaulted crystals is also observed for 4-Br-substituted complex crystal **3f**, which exhibits intense yellow emission under UV excitation at ambient temperature. The quantum efficiencies of the **3f** crystal at 298 and 77 K are 0.20 and 0.47, respectively. In contrast to the 4-Cl and 4-Br complexes, 4-F complex crystal **3e** is non-emissive at ambient temperature, and the quantum efficiencies at 298 and 77 K are <0.01 and 0.49 respectively. The high heat resistance of 4-Cl and 4-Br crystals **3b**, **3f**, and contrasting heat quenchable properties of 4-F crystal **3e** are visualized by the temperature dependent emission spectra (Figs. 2a, 6a and 6b) and the relationship between the normalised intensity of the emission maxima and temperature (Fig. 6c) for these crystals.

### Chromatic controllability with chloro functionality

Chromogenic control can be achieved simply by the introduction of a Cl-substitution at different positions on the aromatic rings. Yellow, orange and red emissions can be generated from the crystals by substitution with a chloro group at the 3-, 4-, 5-, and 6-positions, respectively, whereas the

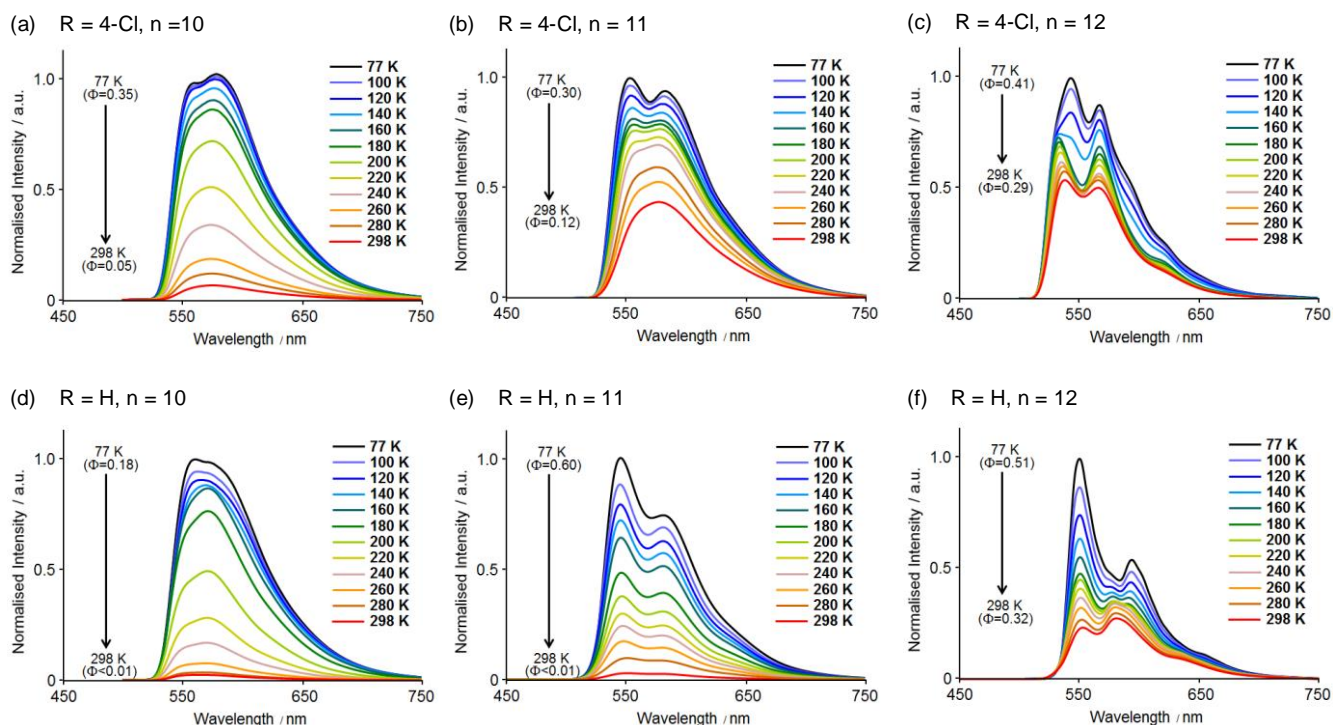


**Fig. 5** Temperature-dependence of emission for (a–c) 4-chloro (**1b–3b**) and (d–e) non-substituted (**1g–3g**) platinum complexes in the crystalline state at 77–298 K ( $\lambda_{\text{ex}} = 420$  nm). Data in c (from Fig. 2a) and d–e (ref. 5a,b) are presented for comparison.

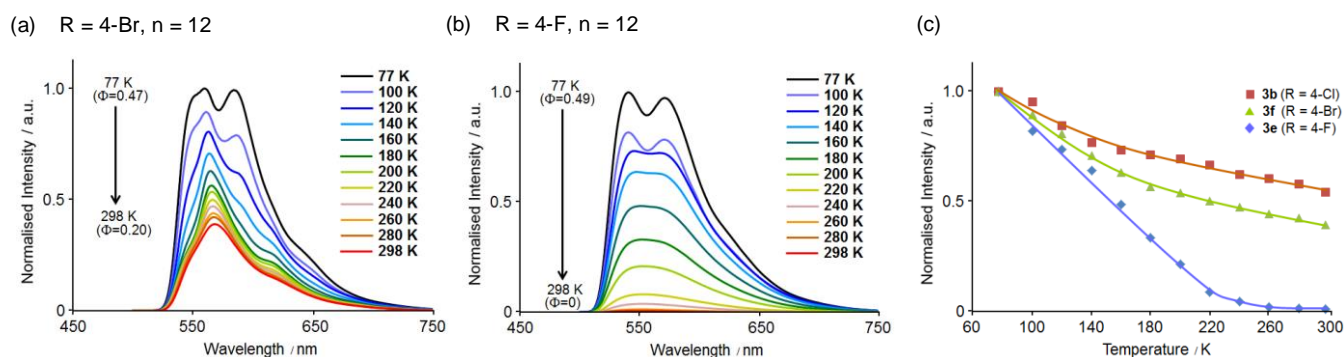


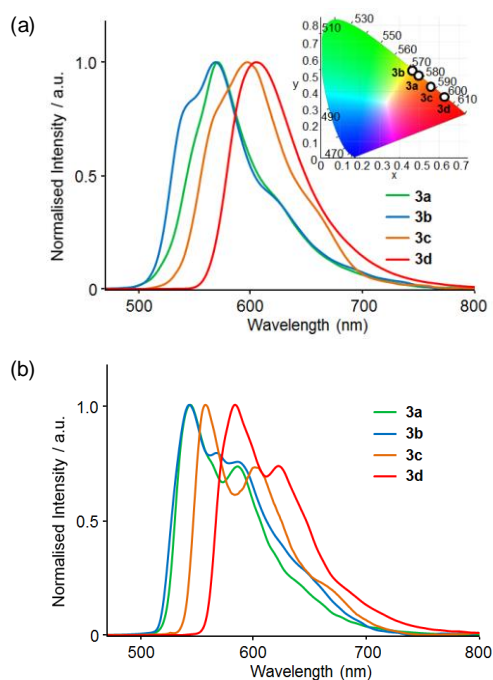
**Fig. 6** Temperature-dependence of emission for (a) heat resistant **3f** and (b) heat quenchable **3e** crystals at 77–298 K ( $\lambda_{\text{ex}} = 420$  nm). (c) Decays in normalised intensity of emission maxima ( $\lambda_{\text{max}}$ ) at 298 K for **3b**, **3e** and **3f** crystals as a function of temperature.

emission colour of the non-substituted crystals **1g–3g** is yellow. Emission spectra of Cl-substituted crystals **3a–d** with dodecamethylene bridges are shown in Fig. 7, where the emission maxima ( $\lambda_{\text{max}}$ ) are significantly varied and dependent on the position of the chloro group [570 (**3a**), 569 (**3b**), 598 (**3c**) and 605 nm (**3d**) at 298 K (Fig. 7a); 544 (**3a**), 543 (**3b**), 557 (**3c**) and 584 nm (**3d**) at 77 K (Fig. 7b)]. The emission maxima of complexes **3a–d** in 2-MeTHF glass state at 77 K are 519 (**3a**), 521 (**3b**), 538 (**3c**) and 538 nm (**3d**) (Table S1, Supplementary Information), which indicates an extraordinary red-shift of the **3d** crystal due to intermolecular interaction in the condensed state. The CIE colour coordinates plotted on the CIE1930 chromaticity chart in Fig. 7a indicate that the

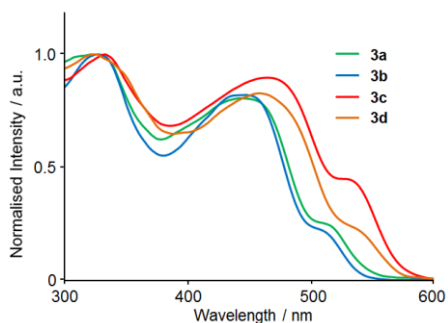
crystalline-state emissions are brilliantly coloured with high chromatic purity. UV-vis diffuse reflectance spectra of **3a–d** have a broad absorption band that is attributable to a mixture of  $^1\text{MLCT}$  (metal-to-ligand charge transfer) and  $^1\text{ILCT}$  (intraligand charge transfer) at approximately 440–460 nm in the crystalline state (Fig. 8). Significant hypsochromic shift in the absorbance of **3a,b** and the bathochromic shift in **3c,d** are rationally synchronized to these changes in emission colour.

#### Mechanistic rationale for solid-state emission enhancement

The contrasting difference in the emission intensities and colours for vaulted **3b** and non-vaulted **4b** crystals (Figs. 2 and 3) can be explained by molecular alignment and intermolecular

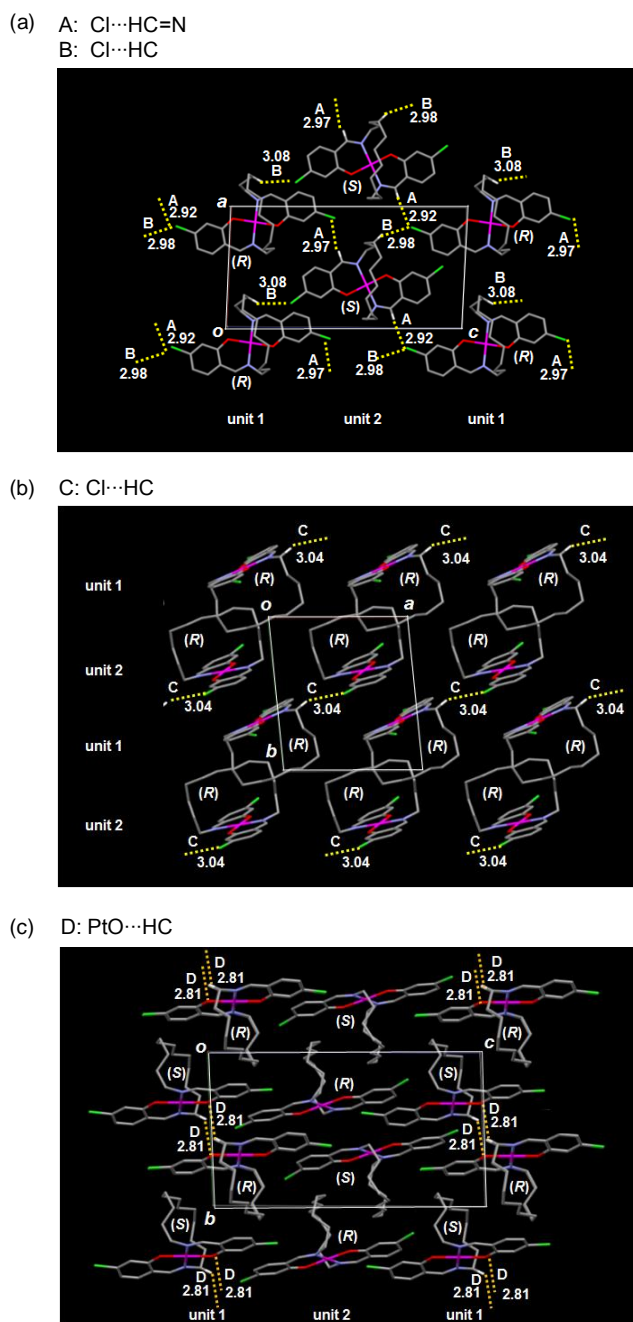


**Fig. 7** Normalised emission spectra for the **3a–d** crystals at (a) 298 and (b) 77 K ( $\lambda_{\text{ex}} = 420$  nm). The inset in (a) shows the CIE colour coordinates of the emissions.



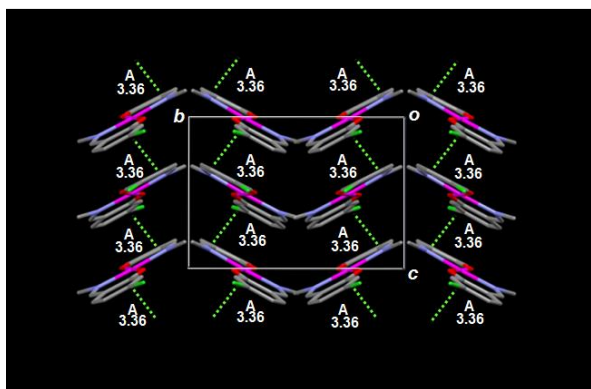
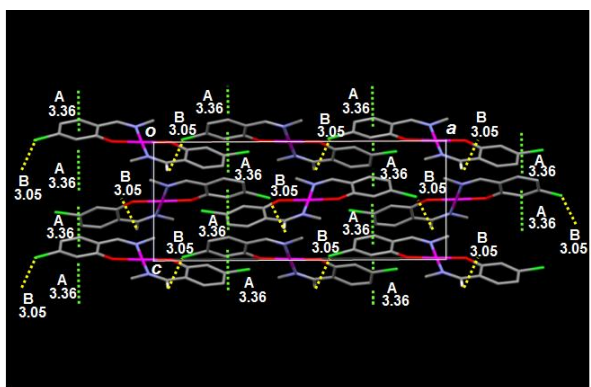
**Fig. 8** Normalised diffuse reflectance UV-vis spectra for the **3a–d** crystals at 298 K ( $\lambda_{\text{ex}} = 420$  nm).

interactions in the crystals. Crystal **3b** has an alternating alignment of the (*R*)-form of unit 1 and (*S*)-form of unit 2 on the *ac*-plane (Fig. 9a) by heterochiral hydrogen-bonding (H-bonding) interactions between Cl and imine H atoms (bonding A), and that between Cl and the linker H (bonding B). The *c*-axis projection (*ab*-plane) of crystal **3b** shows that the *ac*-plane is consecutively stacked with neighbouring *ac*-planes consisting of the (*S*)-form of unit 1 and (*R*)-form of unit 2, where H-bonding between Cl (unit 2) and linker H (unit 1) atoms are observed in a homochiral manner (bonding C in Fig. 9b). Heterochiral H-bonding between O (unit 1) and linker H (unit 1) atoms is also observed on the *bc*-plane (bonding D, Fig. 9c). The *a*-axis projection and overhead view of non-vaulted crystal **4b** show that the aromatic moiety of each molecular unit is stacked consecutively with a typical  $\pi$ -stacking distance [the distance between C(1)–C(6)–C(5) and C(2')–C(3')–C(4') planes] of 3.36 Å to give a highly regulated multilayered structure (bonding A in Figs. 10a and b). H-bonding between

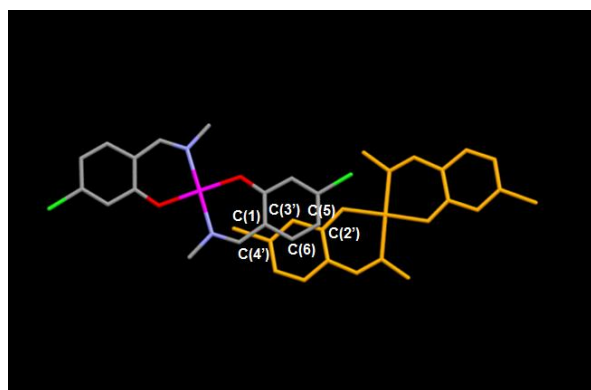


**Fig. 9** Packing and significant interactions in the **3b** crystal. (a) *b*-, (b) *c*- and (c) *a*-axis projections.

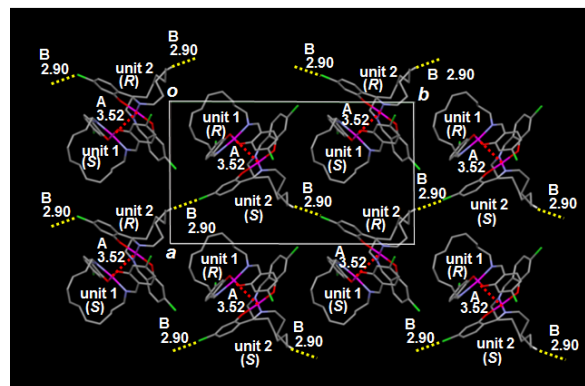
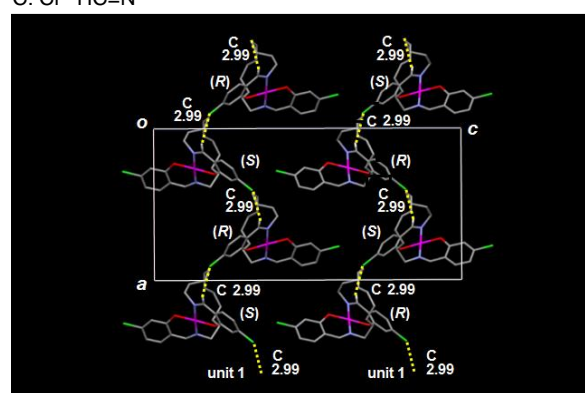
Cl and imine H atoms is observed on the *ac*-plane as the sole significant H-bonding interaction in crystal **4b** (bonding B in Fig. 10b). These results indicate that vaulted complex **3b** has three-dimensional (3D) molecular constraint in the crystalline state, while non-vaulted crystal **4b** is less bound with stacking and H-bonding interactions in a 2D manner. Thus, the contrasting heat resistance properties of crystals **3b** ( $\Phi_{298\text{K}}/\Phi_{77\text{K}} = 0.71$ ) and **4b** ( $<0.01$ ) are attributable to the degree of dimensionality in molecular constraint of the crystal unit, which would significantly inhibit the dispersion of photoenergy from the excited state at higher temperature.<sup>5</sup> The low quantum

(a) A:  $\pi$ -stacking(b) A:  $\pi$ -stacking  
B: Cl $\cdots$ HC=N

(c)

**Fig. 10** Packing and significant interactions in the **4b** crystal. (a) *a*- and (b) *b*-axis projections. (c) Overhead view of a stacked dimer.

efficiency of crystal **4b** observed even at 77 K ( $\Phi_{77\text{K}} = 0.12$ , Table 2) can be rationalized by the energy dispersion through consecutive intermolecular  $\pi$ -stacking interactions of aromatic rings. The correlation between the low emission properties and consecutive stacking molecular array in the crystalline state has been discussed for non-vaunted *trans*-bis(salicylaldiminato)platinum complexes bearing long alkyl chains.<sup>5c</sup> The specific red-shifted emission of the **4b** crystal (Fig. 3) can be also attributed to highly regulated  $\pi$ -stacking,<sup>11</sup> as shown in Fig. 10a.

(a) A: Pt $\cdots$ Pt  
B: Cl $\cdots$ HC(b) C: Cl $\cdots$ HC=N**Fig. 11** Packing and significant interactions in the **2b** crystal. (a) *c*- and (b) *b*-axis projections.

Low structural dependence on the heat resistance properties of 4-Cl-substituted crystals **1b–3b** (Fig. 4) can also be rationalized by their higher dimensionality of molecular constraint in the crystal unit. As shown by the packing of the short-vaunted **2b** crystal ( $n = 11$ , Fig 11a), cofacial pairs of (*R*)-unit 1 and (*S*)-unit 2, bound with Pt $\cdots$ Pt interaction (bonding A) are aligned alternatively with their enantiomeric pairs of (*S*)-unit 1 and (*R*)-unit 2, with H-bonding interactions between Cl and linker H atoms (bonding B). Heterochiral H-bonding interactions between Cl and imine H atoms of identical units are also observed on the *ac*-plane of the crystal (bonding C in Fig. 11b). These results indicate that even short-vaunted crystal **2b** has a similar high dimensionality of self-constraint in the molecular unit, as with long-vaunted crystal **3b**, due to the significant contribution of Cl substituents to the self-constraint of the crystal unit. This is in contrast to the difference in the packing of non-substituted crystals, where the long-vaunted **3g** unit has 3D self-constraint with various O $\cdots$ H and Pt $\cdots$ Pt interactions due to its highly planar structure, while the short-vaunted units **1g** and **2g** have low dimensionality in self-constraint arising from their bent structures.<sup>5a,b</sup> Thus, the enhancement of such self-constraint by Cl-substitution leads to a decrease in the clear structure-dependence of the heat resistance/quenchable properties of **1g–3g** crystals (Fig. 4b). The comparably high heat resistance of 4-Br-substituted

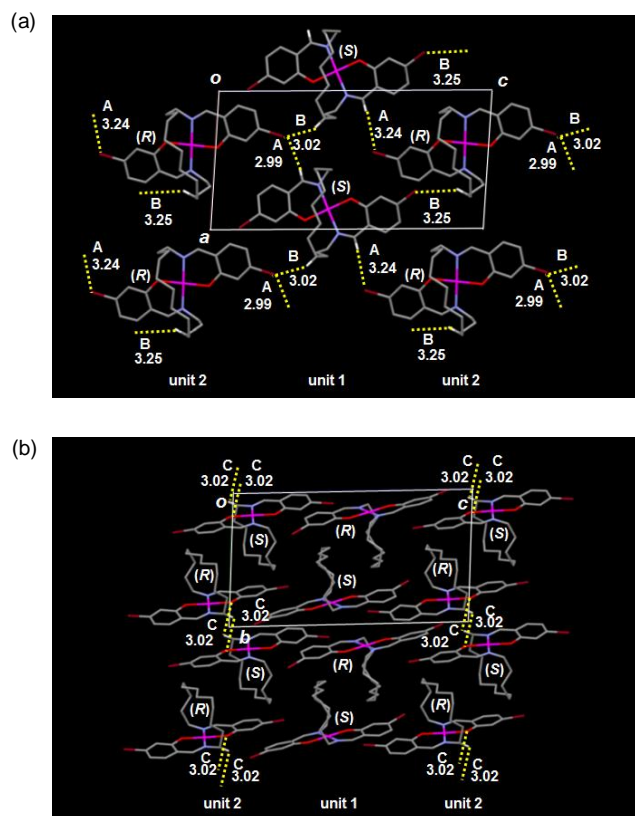


**Fig. 12** Packing and significant interactions in the **3f** crystal. (a) *b*- and (b) *a*-axis projections.

crystal **3f** (Fig. 6a) is also ascribed to a high dimensionality of molecular constraint in the crystal unit, similar to that of 4-Cl analogue **3b** (Figs. 9 and 12). Heat quenchable 4-F crystal **3e** (Figs. 6b and c) has an alternating alignment of (*R*)- and (*S*)-units, which are bound to each other with H-bonding interactions between F and imine H atoms (Fig. 13). This singular interaction on the *ac*-plane is the sole significant intermolecular interaction in crystal **3e**. Such a low dimensionality of molecular constraint in the crystal unit would induce the heat quenchable properties of the **3e** crystal.

The molecular orbitals of **3a–d** were estimated from density functional theory (DFT; B3LYP/6-31\*G, LanL2DZ) calculations on the basis of the optimized structures. The highest-occupied molecular orbitals (HOMO) of all complexes are principally Pt(5d)–O(2p) hybrids, while the lowest-unoccupied molecular orbitals (LUMO) are C=N ( $\pi^*$ ) (Fig. S1, Supplementary Information). The energy levels and electronic configurations of the singlet and triplet states of **3a–d** were estimated from time-dependent DFT (TD-DFT) calculations (Table S3, Supplementary Information). The major electronic configuration of the  $S_1(T_1)$  states are determined to be HOMO-to-LUMO, which implies that the present phosphorescent emission is principally attributable to  $^3MLCT$ . Chromatic control by chloro functionalization was rationalized on the basis of these calculations and the molecular packing in the crystals. The maximum emission wavelengths of **3a–d**, observed in a diluted 2-MeTHF glass state at 77 K, are strongly correlated to the  $T_1-S_0$  gaps [2.35 (**3a**), 2.38 (**3b**), 2.25 (**3c**), 2.30 eV (**3d**)] estimated from TD-DFT calculations (Fig. S2, Supplementary Information). Given the conclusion that the major electronic

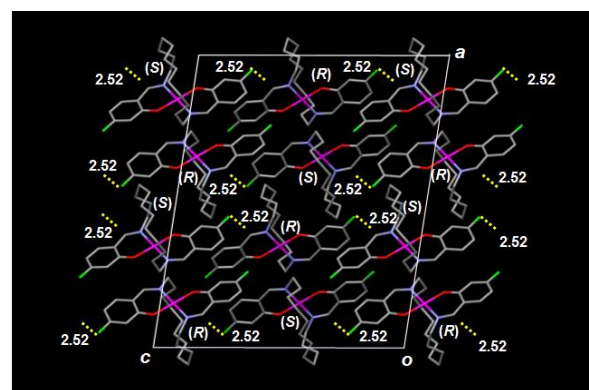


**Fig. 13** Packing and significant interactions in the **3e** crystal. *b*-Axis projection.

- (a) A:  $\pi$ -stacking  
 B: Cl $\cdots$ HC  
 C: O $\cdots$ HC

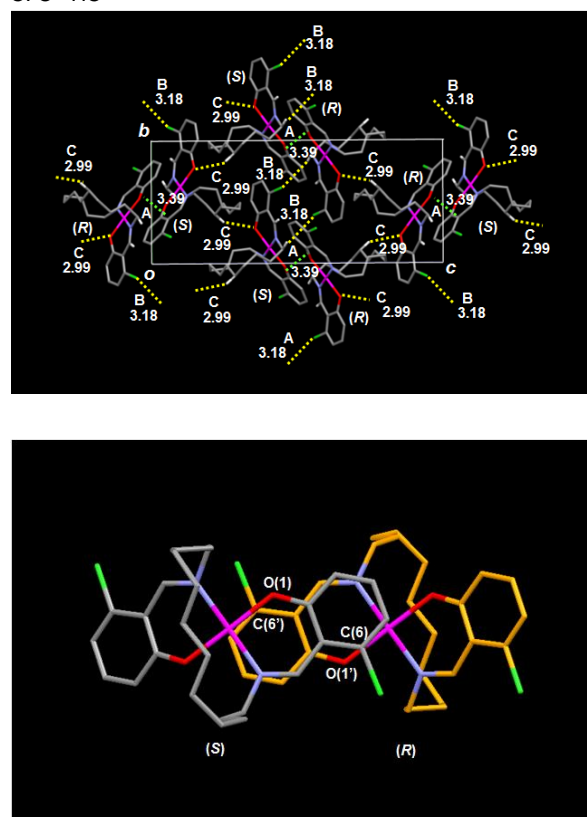


**Fig. 14** Packing and significant interactions in the **3d** crystal. (a) *a*-Axis projection. (b) Overhead view of heterochiral stacked dimer.

configuration of the  $S_1(T_1)$  states are HOMO-to-LUMO, this correlation indicates that the present chromatic changeability in the diluted glass state can be explained simply based on the frontier orbitals of an isolated system. The significant red-shift of the emission from 6-Cl crystal **3d** (Fig. 7b) is ascribed to its specific  $\pi$ -stacking interaction between crystal units. The *a*-

axis projection of the **3d** crystal shows that cofacial dimeric pairs of (*R*)- and (*S*)-units bound with  $\pi$ -stacking interaction (bonding A) are aligned in an alternatively overturned packing manner with the assistance of H-bonding interactions (bondings B and C) (Fig. 14a). The overhead view of the heterochiral dimer unit clearly shows the deep stacking situation where electron-rich sites around O(1)/O'(1) atoms are bound with electron-deficient sites around C(6)/C'(6) atoms in a head-to-tail manner. Such strong donor-acceptor interactions would induce significant red-shift of the emission in the crystalline state (Fig. 3a).<sup>12</sup>

Figure 15 shows schematic representations for the effect of Cl-substitution on the packing and emission properties of long- and short-vaulted crystals **2** and **3**. The high coordination planarity and strong Pt $\cdots$ Pt interactions provide the long-vaulted ( $n = 12$ ), non-substituted crystal **3g** with high emission properties at 77 K and heat resistance towards emission decay at higher temperature (Fig. 15a, left).<sup>5a,b</sup> The Cl $\cdots$ H bonding network in the 4-Cl-substituted, long-vaulted ( $n = 12$ ) **3b** crystal takes precedence with sacrifice of the advantageous Pt $\cdots$ Pt interactions to maximize the total stabilization of the crystal unit. Thus, the emission and heat resistance properties of crystal **3b** remain high after Cl-substitution, due to the high coordination planarity and high dimensionality of molecular constraint (Fig. 15a, right). The short-vaulted ( $n = 11$ ), non-

substituted **2g** crystal has no significant intermolecular interactions such as H-bonding or Pt $\cdots$ Pt contact, which affords extraordinarily low heat resistance properties (Fig. 15b, left).<sup>5a,b</sup> Cl-substitution of the short-vaulted complex ( $n = 11$ ) increases self-constraint in the crystal unit by the addition of two-dimensional Cl $\cdots$ H bonding and Pt $\cdots$ Pt interactions with a decrease in the coordination planarity of the crystal unit (Fig. 15b, right). This change in the structure and environment of the crystal unit induces not only a decrease in quantum efficiency at 77 K ( $\Phi_{77K}$ : 0.60 for **2g**<sup>5a,b</sup> 0.30 for **2b**), but also an increase in the heat resistance properties ( $\Phi_{298K}/\Phi_{77K}$ : < 0.01 for **2g**<sup>5a,b</sup> and 0.40 for **2b**).

It should be noted that Cl-substitution of non-vaulted crystal **4** significantly decreases the heat resistance towards emission decay ( $\Phi_{298K}/\Phi_{77K}$ : 0.53 for **4g**<sup>5a,b</sup> and 0.08 for **4b**). This contrasting phenomenon can also be rationalized by the Cl $\cdots$ H bonding, which acts as an important supporting factor for the construction of a low dimensional stacking architecture, as shown in Fig. 10b. These results suggest that the emission enhancement with halogen functionalization is the result of a synergistic effect caused by the strong H-bonding ability of halogen atoms and the specific 3D superstructure of the vaulted crystal unit.

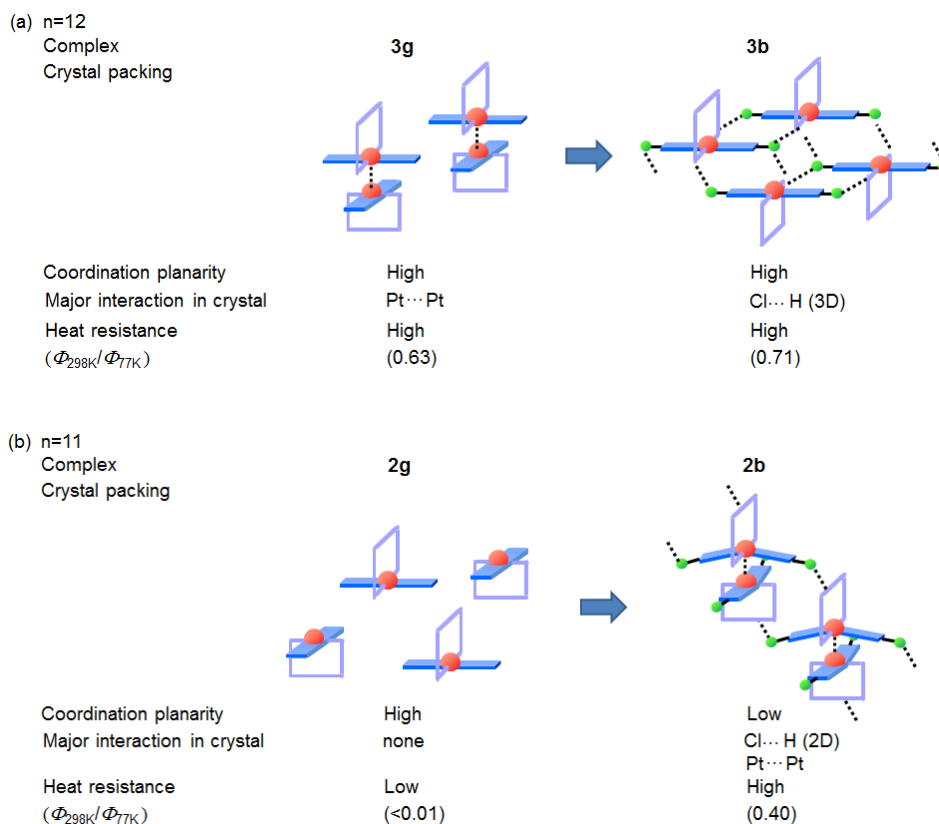


Fig. 15 Schematic representation of the Cl-substitution effect on (a) long- and (b) short-vaulted crystals.

## Conclusions

A series of polymethylene-vaulted *trans*-bis(salicylaldiminato)platinum(II) complexes bearing halogen functionalities was synthesized that exhibits intense emissions in the crystalline state. Chloro-substitution has proven to significantly increase the lower heat resistance of short-vaulted, non-substituted crystals, and maintain the intense emission of long-vaulted analogues, which leads to intense solid-state emission of the vaulted crystals with low structural dependence. XRD studies have revealed that the emission enhancement with halogen functionalization is due to an increase in the dimensionality of molecular constraint in the crystal unit due to a synergistic effect of the vaulted structure and highly dimensional H-bonding network interactions.

## Experimental section

### General

*N,N'*-Bis(salicylidene)-1, $\omega$ -alkanediamines were prepared by reaction of substituted salicylaldehyde (3-Cl,<sup>13</sup> 4-Cl,<sup>14</sup> 5-Cl, 6-Cl,<sup>14</sup> 4-Br and 4-F) with 1, $\omega$ -alkanediamine ( $\omega$  = 10–12) in boiling ethanol. Melting points were measured in a glass capillary on a Büchi B-545 melting point apparatus. IR spectra were recorded on a Bruker Equinox 55/S spectrometer. <sup>1</sup>H and <sup>13</sup>C NMR spectra were recorded on a Varian Unity-Inova 500 spectrometer. Mass spectra were obtained on a Jeol JMS-DX 303 spectrometer. Elemental analyses were performed with a Perkin-Elmer 2400II CHN elemental analyser. Diffuse reflectance UV-vis spectra were obtained on a Jasco V-570 spectrometer equipped with an integrating sphere. Emission spectra were obtained using a Jasco FP-6500 spectrometer. Quantum efficiencies were measured by the absolute method<sup>11</sup> using a Jasco FP-6500 spectrometer equipped with an integrating sphere. Emission lifetime measurements were conducted using an Optical Building Blocks EasyLife V instrument with a 415 nm LED for excitation.

### Synthesis of platinum complexes 1–3.

A mixture of PtCl<sub>2</sub>(CH<sub>3</sub>CN)<sub>2</sub><sup>15</sup> (0.423 g, 1.00 mmol), the corresponding *N,N'*-bis(salicylidene)-1, $\omega$ -alkanediamine (1.00 mmol), and K<sub>2</sub>CO<sub>3</sub> (0.900 g, 6.51 mmol) in DMSO (60 mL) was refluxed with toluene (240 mL) at 140 °C for 24 h. After evaporation of the solvent under reduced pressure, the residue was poured into a mixture of EtOAc (20 mL) and water (200 mL). The resulting organic layer was washed with water, dried over MgSO<sub>4</sub>, and concentrated under reduced pressure to give a crude orange solid. Column chromatography (Fuji Silysia Chromatorex NH-DM1020, *n*-hexane/EtOAc) afforded 1–3 as a yellow or orange solid. The complexes were recrystallized from EtOH for photophysical studies (Table 2, Figs. 2–8).

**Complex 1b.** Yellow block (1.1%). mp 214–215 °C. IR (KBr) 2928, 2854, 1622, 1593, 1524, 1458, 1423, 1392, 1293, 1201, 1075, 937, 857, 782 cm<sup>-1</sup>; <sup>1</sup>H NMR (CDCl<sub>3</sub>, 500 MHz)  $\delta$  1.20–1.83 (m, 14 H), 2.37–2.47 (m, 2 H), 2.97 (ddd,  $J$  = 11.4, 10.8, 3.4 Hz, 2 H), 4.84 (ddd,  $J$  = 11.4, 3.9, 3.9 Hz, 2 H), 6.56 (dd,  $J$  = 8.5, 2.0 Hz, 2 H), 6.90 (d,  $J$  = 2.0 Hz, 2 H), 7.14 (d,  $J$  = 8.5 Hz, 2 H), 7.74 (s, 2 H); <sup>13</sup>C NMR (CDCl<sub>3</sub>, 125 MHz)  $\delta$  22.9, 25.7, 27.3, 28.7, 59.6, 116.4, 119.8, 119.9, 134.2, 139.0, 157.6, 164.1; HRMS (FAB<sup>+</sup>)  $m/z$  calcd for C<sub>24</sub>H<sub>28</sub>N<sub>2</sub>O<sub>2</sub><sup>35</sup>Cl<sup>37</sup>Cl<sup>194</sup>Pt (M<sup>+</sup>): 642.1125; found: 642.1099.

**Complex 2b.** Yellow platelets (35%). mp 210–211 °C. IR (KBr) 2924, 2853, 1621, 1593, 1524, 1425, 1393, 1295, 1200, 1074, 932, 854, 780 cm<sup>-1</sup>; <sup>1</sup>H NMR (CDCl<sub>3</sub>, 500 MHz)  $\delta$  1.20–1.64 (m, 16 H), 2.20–2.30 (m, 2 H), 2.85 (ddd,  $J$  = 11.4, 10.0, 2.7 Hz, 2 H), 4.84 (ddd,  $J$  = 11.4, 3.9, 3.9 Hz, 2 H), 6.56 (dd,  $J$  = 8.5, 2.0 Hz, 2 H), 6.88 (d,  $J$  = 2.0 Hz, 2 H), 7.13 (d,  $J$  = 8.5 Hz, 2 H), 7.70 (s, 2 H); <sup>13</sup>C NMR (CDCl<sub>3</sub>, 125 MHz)  $\delta$  23.8, 26.2, 27.2, 27.9, 30.4, 58.9, 116.5, 119.8, 119.9, 134.2, 139.1, 158.0, 164.3; HRMS (FAB<sup>+</sup>)  $m/z$  calcd for C<sub>25</sub>H<sub>30</sub><sup>35</sup>Cl<sub>2</sub>N<sub>2</sub>O<sub>2</sub><sup>196</sup>Pt: 656.1334 (M<sup>+</sup>); found: 656.1337.

**Complex 3a.** Yellow block (5.9%). mp 229–230 °C. IR (KBr) 2924, 2849, 1619, 1594, 1441, 1404, 1325, 1228, 1187, 1142, 1079, 866, 734 cm<sup>-1</sup>; <sup>1</sup>H NMR (CDCl<sub>3</sub>, 500 MHz)  $\delta$  1.10–1.50 (m, 18 H), 2.22–2.33 (m, 2 H), 2.99 (ddd,  $J$  = 11.2, 10.4, 3.0 Hz, 2 H), 5.24 (ddd,  $J$  = 11.2, 4.3, 4.3 Hz, 2 H), 6.55 (dd,  $J$  = 7.8, 7.8 Hz, 2 H), 7.19 (dd,  $J$  = 7.8, 1.6 Hz, 2 H), 7.48 (dd,  $J$  = 7.8, 1.6 Hz, 2 H), 7.87 (s, 2 H); <sup>13</sup>C NMR (CDCl<sub>3</sub>, 125 MHz)  $\delta$  23.2, 27.0, 27.4, 27.5, 29.9, 59.7, 115.3, 121.6, 124.6, 132.4, 133.1, 158.2, 158.4; HRMS (FAB<sup>+</sup>)  $m/z$  calcd for C<sub>26</sub>H<sub>32</sub>N<sub>2</sub>O<sub>2</sub><sup>35</sup>Cl<sub>2</sub><sup>196</sup>Pt (M<sup>+</sup>): 670.1490; found: 670.1473.

**Complex 3b.** Yellow block (23%). mp 200–201 °C. IR (KBr) 2926, 2850, 1617, 1524, 1429, 1301, 1208, 1074, 932, 777 cm<sup>-1</sup>; <sup>1</sup>H NMR (CDCl<sub>3</sub>, 500 MHz)  $\delta$  1.08–1.18 (m, 2 H), 1.26–1.53 (m, 16 H), 2.10–2.21 (m, 2 H), 2.92 (ddd,  $J$  = 11.2, 10.3, 3.1 Hz, 2 H), 4.86 (ddd,  $J$  = 11.2, 4.5, 4.5 Hz, 2 H), 6.57 (dd,  $J$  = 8.5, 1.8 Hz, 2 H), 6.90 (d,  $J$  = 1.8 Hz, 2 H), 7.15 (d,  $J$  = 8.5 Hz, 2 H), 7.77 (s, 2 H); <sup>13</sup>C NMR (CDCl<sub>3</sub>, 125 MHz)  $\delta$  23.4, 27.1, 27.4, 27.5, 29.9, 58.8, 116.5, 119.4, 119.9, 134.3, 139.1, 158.1, 163.9. Anal. calcd for C<sub>26</sub>H<sub>32</sub>Cl<sub>2</sub>N<sub>2</sub>O<sub>2</sub>Pt: C, 46.58; H, 4.81; N, 4.18. Found: C, 46.64; H, 4.68; N, 4.15.

**Complex 3c.** Orange block (25%); mp 235–236 °C; IR (KBr) 2923, 2852, 1619, 1530, 1461, 1391, 1315, 1178, 1135, 818, 705 cm<sup>-1</sup>; <sup>1</sup>H NMR (CDCl<sub>3</sub>, 500 MHz)  $\delta$  1.07–1.18 (m, 2 H), 1.25–1.54 (m, 16 H), 2.11–2.21 (m, 2 H), 2.92 (ddd,  $J$  = 11.2, 10.2, 3.2 Hz, 2 H), 4.88 (ddd,  $J$  = 11.2, 4.1, 4.1 Hz, 2 H), 6.82 (d,  $J$  = 8.9 Hz, 2 H), 7.20 (d,  $J$  = 2.7 Hz, 2 H), 7.24 (dd,  $J$  = 8.9, 2.7 Hz, 2 H), 7.75 (s, 2 H); <sup>13</sup>C NMR (CDCl<sub>3</sub>, 125 MHz)  $\delta$  23.4, 27.1, 27.3, 27.5, 29.9, 58.9, 119.8, 121.1, 121.9, 131.6, 133.5, 157.8, 162.3; HRMS (FAB<sup>+</sup>)  $m/z$  calcd for C<sub>26</sub>H<sub>32</sub><sup>35</sup>Cl<sub>2</sub>N<sub>2</sub>O<sub>2</sub><sup>196</sup>Pt (M<sup>+</sup>): 670.1490; found: 670.1473.

**Complex 3d.** Orange solid (3.2%). mp 187.0–188.0 °C; IR (KBr) 2926, 2854, 1612, 1594, 1527, 1438, 1397, 1350, 1315, 1192, 950, 919, 781, 722 cm<sup>-1</sup>; <sup>1</sup>H NMR (CDCl<sub>3</sub>, 500 MHz)  $\delta$  1.12–1.64 (m, 18 H), 2.15–2.25 (m, 2 H), 3.08 (ddd,  $J$  = 11.2, 10.3, 3.9 Hz, 2 H), 4.88 (ddd,  $J$  = 11.2, 5.0, 5.0 Hz, 2 H), 6.64 (dd,  $J$  = 7.6, 1.1 Hz, 2 H), 6.80 (dd,  $J$  = 8.6, 1.1 Hz, 2 H), 7.15 (dd,  $J$  = 8.6, 7.6 Hz, 2 H), 8.41 (s, 2 H); <sup>13</sup>C NMR (CDCl<sub>3</sub>, 125 MHz)  $\delta$  23.9, 27.2, 27.3, 27.7, 30.4, 59.4, 117.0, 118.5, 119.8, 132.4, 135.4, 155.9, 165.6; HRMS (FAB<sup>+</sup>)  $m/z$  calcd for C<sub>26</sub>H<sub>32</sub>N<sub>2</sub>O<sub>2</sub><sup>35</sup>Cl<sup>37</sup>Cl<sup>195</sup>Pt (M<sup>+</sup>): 671.1459; found: 671.1461.

**Complex 3e.** Yellow block (34%). mp 172–173 °C; IR (KBr) 2930, 2854, 1623, 1544, 1434, 1301, 1216, 1155, 1114, 989, 850 cm<sup>-1</sup>; <sup>1</sup>H NMR (CDCl<sub>3</sub>, 500 MHz)  $\delta$  1.08–1.18 (m, 2 H), 1.27–1.54 (m, 16 H), 2.12–2.22 (m, 2 H), 2.91 (ddd,  $J$  = 11.3, 10.4, 3.4 Hz, 2 H), 4.84 (ddd,  $J$  = 11.3, 4.4, 4.4 Hz, 2 H), 6.35 (ddd,  $J$  = 8.7, 7.8, 2.5 Hz, 2 H), 6.55 (dd,  $J$  = 11.7, 2.5 Hz, 2 H), 7.20 (dd,  $J$  = 8.7, 7.1 Hz, 2 H), 7.75 (s, 2 H); <sup>13</sup>C NMR (CDCl<sub>3</sub>, 125 MHz)  $\delta$  23.4, 27.1, 27.4, 27.5, 29.9, 58.7, 104.8 (d, <sup>2</sup>J<sub>C-F</sub> = 24 Hz), 105.5 (d, <sup>2</sup>J<sub>C-F</sub> = 20 Hz), 135.3 (d, <sup>3</sup>J<sub>C-F</sub> = 12 Hz), 117.9, 158.0, 165.3 (d, <sup>3</sup>J<sub>C-F</sub> = 14 Hz), 166.2 (d, <sup>1</sup>J<sub>C-F</sub> = 252 Hz); HRMS (FAB<sup>+</sup>)  $m/z$  calcd for C<sub>26</sub>H<sub>32</sub>F<sub>2</sub>N<sub>2</sub>O<sub>2</sub><sup>195</sup>Pt (M<sup>+</sup>): 637.2080; found: 637.2063.

**Complex 3f.** Yellow block (27%). mp 220–221 °C. IR (KBr) 2925, 2850, 1618, 1587, 1523, 1429, 1398, 1340, 1299,

1208, 1063, 917, 777  $\text{cm}^{-1}$ ;  $^1\text{H}$  NMR ( $\text{CDCl}_3$ , 500 MHz)  $\delta$  1.07–1.19 (m, 2 H), 1.26–1.52 (m, 16 H), 2.10–2.22 (m, 2 H), 2.91 (ddd,  $J = 11.2, 10.7, 3.1$  Hz, 2 H), 4.83 (ddd,  $J = 11.2, 4.5, 4.5$  Hz, 2 H), 6.71 (dd,  $J = 8.3, 2.0$  Hz, 2 H), 7.08 (d,  $J = 8.3$  Hz, 2 H), 7.08 (d,  $J = 2.0$  Hz, 2 H), 7.76 (s, 2 H);  $^{13}\text{C}$  NMR ( $\text{CDCl}_3$ , 125 MHz)  $\delta$  23.4, 27.1, 27.4, 27.5, 29.8, 58.9, 119.2, 119.7, 123.0, 127.8, 134.3, 158.2, 163.8; HRMS (FAB $^+$ )  $m/z$  calcd for  $\text{C}_{26}\text{H}_{32}\text{N}_2\text{O}_2^{79}\text{Br}^{81}\text{Br}^{195}\text{Pt}$  ( $\text{M}^+$ ): 759.0458; found: 759.0446.

**Complex 4b.** Similar treatment of  $\text{PtCl}_2(\text{CH}_3\text{CN})_2$  with *N*-(4-chlorosalicylidene)methylamine (2 equiv.) gave an orange block (12%). mp >290 °C; IR (KBr) 2916, 1624, 1590, 1523, 1426, 1298, 1203, 1146, 1073, 938, 773  $\text{cm}^{-1}$ ;  $^1\text{H}$  NMR ( $\text{DMSO}-d_6$ , 500 MHz)  $\delta$  3.52 (s, 6 H), 6.68 (dd,  $J = 8.7, 1.8$  Hz, 2 H), 6.96 (d,  $J = 1.8$  Hz, 2 H), 7.47 (d,  $J = 8.7$  Hz, 2 H), 8.37 (s, 2 H);  $^{13}\text{C}$  NMR ( $\text{CDCl}_3/\text{CD}_3\text{OD}$ , 125 MHz)  $\delta$  70.0, 116.7, 119.2, 119.8, 134.2, 139.2, 159.0, 163.3; HRMS (FAB $^+$ )  $m/z$  calcd for  $\text{C}_{16}\text{H}_{14}^{35}\text{Cl}_2\text{N}_2\text{O}_2^{194}\text{Pt}$  ( $\text{M}^+$ ): 530.0059; found: 530.0074.

**X-ray structure determination.** Crystals suitable for XRD studies were analyzed using a Rigaku R-AXIS RAPID imaging plate diffractometer with graphite-monochromated Mo  $\text{K}\alpha$  radiation ( $\lambda = 0.71075$  Å). The structures of ( $\pm$ )-**2b**, ( $\pm$ )-**3b**, ( $\pm$ )-**3c**, ( $\pm$ )-**3d**, ( $\pm$ )-**3e**, ( $\pm$ )-**3f**, and **4b** were solved using direct methods and refined with the full-matrix least-squares method. In subsequent refinement, the function  $\sum \omega(F_o^2 - F_c^2)^2$  was minimized, where  $F_o$  and  $F_c$  are the observed and calculated structure factor amplitudes, respectively. The positions of non-hydrogen atoms were determined from difference Fourier electron density maps and refined anisotropically. All calculations were performed using the Crystal Structure crystallographic software package, and illustrations were drawn using ORTEP.<sup>10</sup> Details of the structure determinations are given in Fig. 1 and Table 1. CCDC-985138 (**2b**), 985139 (**3b**), 985140 (**3c**), 985141 (**3d**), 985142 (**3e**), 985143 (**3f**), and 985144 (**4b**) contain the supplementary crystallographic data for this paper. These data can be obtained free of charge from The Cambridge Crystallographic Data Centre via [www.ccdc.cam.ac.uk/data\\_request/cif](http://www.ccdc.cam.ac.uk/data_request/cif).

**Computational methods.** All calculations were conducted on the basis of DFT with the B3LYP exchange-correlation functional<sup>16</sup> and using the Gaussian 09W program package.<sup>17</sup> The basis set used was the effective core potential (LanL2DZ) for a platinum atom<sup>18</sup> and 6-31G\* for the remaining atoms.<sup>19</sup> Molecular orbitals and their eigenvalues for complexes **3a–d** were calculated using the optimized molecular structures. The singlet–singlet ( $E(S_n)$ ) and singlet–triplet ( $E(T_n)$ ) transition energies were estimated by TD-DFT calculation (B3LYP/6-31G\*, LanL2DZ).<sup>20</sup> The results are shown in Fig. S1 and Table S3, Supplementary Information.

## Acknowledgements

This work was supported by a Grant-in-Aid for Scientific Research, from the Ministry of Education, Culture, Sports, Science and Technology, Japan. We gratefully acknowledge Mr. Masahiko Bando (Otsuka Pharmaceutical Co. Ltd., Japan) for assistance with the X-ray crystallographic analysis of **4b**.

## Notes and references

Department of Chemistry, Graduate School of Engineering Science, Osaka University, Machikaneyama, Toyonaka, Osaka 560-8531, Japan.  
E-mail: [naota@chem.es.osaka-u.ac.jp](mailto:naota@chem.es.osaka-u.ac.jp)

† Electronic supplementary information (ESI) available: Photophysical data of **1–4** in 2-MeTHF; Photophysical data of **1g**, **2g**, and **3g** in crystalline state; Frontier orbitals and their eigenvalues for **3a–d**; excitation energy, oscillator strength and major electronic configuration of **3a–d**; relationship between the  $T_1$ – $S_0$  energy gap and  $\lambda_{\text{max}}$  for **3a–d** in 2-MeTHF at 77 K. See DOI: 10.1039/b000000x/

- (a) R. C. Evans, P. Douglas and C. J. Winscom, *Coord. Chem. Rev.*, 2006, **250**, 2093–2126; (b) *Highly Efficient OLEDs with Phosphorescent Materials*, H. Yersin, ed., Wiley-VCH, Weinheim, 2008; (c) H. Yersin, A. F. Rausch, R. Czerwieniec, T. Hofbeck and T. Fischer, *Coord. Chem. Rev.*, 2011, **255**, 2622–2652; (d) L. Xiao, Z. Chen, B. Qu, J. Luo, S. Kong, Q. Gong and J. Kido, *Adv. Mater.*, 2011, **23**, 926–952.
- Pt: (a) C. E. Buss and K. R. Mann, *J. Am. Chem. Soc.*, 2002, **124**, 1031–1039; (b) M. Kato, A. Omura, A. Toshikawa, S. Kishi and Y. Sugimoto, *Angew. Chem. Int. Ed.*, 2002, **41**, 3183–3185; (c) L. J. Grove, J. M. Rennekamp, H. Jude and W. B. Connick, *J. Am. Chem. Soc.*, 2004, **126**, 1594–1595; (d) T. J. Wadas, Q.-M. Wang, Y. Kim, C. Flaschenreim, T. N. Blanton and R. Eisenberg, *J. Am. Chem. Soc.*, 2004, **126**, 16841–16849; (e) Y. Sun, K. Ye, H. Zhang, J. Zhang, L. Zhao, B. Li, G. Yang, B. Yang, Y. Wang, S.-W. Lai and C.-M. Che, *Angew. Chem. Int. Ed.*, 2006, **45**, 5610–5613; Au (f) M. A. Rawashdeh-Omary, M. A. Omary, J. P. Fackler, Jr., R. Galassi, B. R. Pietroni and A. Burini, *J. Am. Chem. Soc.*, 2001, **123**, 9689–9691; (g) S. H. Lim, M. M. Olmstead and A. L. Balch, *J. Am. Chem. Soc.*, 2011, **133**, 10229–10238; (h) M. A. Malwitz, S. H. Lim, R. L. White-Morris, D. M. Pham, M. M. Olmstead, A. L. Balch, *J. Am. Chem. Soc.* 2012, **134**, 10885–10893; Au–Ag (i) A. Laguna, T. Lasanta, J. M. López-de-Luzuriaga, M. Monge, P. Naumov and M. E. Olmos, *J. Am. Chem. Soc.*, 2010, **132**, 456–457; (j) T. Lasanta, M. E. Olmos, A. Laguna, J. M. López-de-Luzuriaga and P. Naumov, *J. Am. Chem. Soc.*, 2011, **133**, 16358–16361; Au–Ti (k) E. J. Fernández, J. M. López-de-Luzuriaga, M. Monge, M. E. Olmos, J. Pérez, A. Laguna, A. A. Mohamed and J. P. Fackler, Jr. *J. Am. Chem. Soc.*, 2003, **125**, 2022–2023; Au–Cu (l) I. O. Koshevoy, Y.-C. Chang, A. J. Karttunen, M. Haukka, T. Pakkanen and P.-T. Chou, *J. Am. Chem. Soc.*, 2012, **134**, 6564–6567; (m) G. F. Manbeck, W. W. Brennessel, R. A. Stockland, Jr., R. Eisenberg, *J. Am. Chem. Soc.* 2010, **132**, 12307–12318.
- Review (a) A. L. Balch, *Angew. Chem., Int. Ed.*, 2009, **48**, 2641–2644; Au (b) Y. Lee and R. Eisenberg, *J. Am. Chem. Soc.*, 2003, **125**, 7778–7779; (c) H. Ito, T. Saito, N. Oshima, N. Kitamura, S. Ishizaka, Y. Hinatsu, M. Wakeshima, M. Kato, K. Tsuge and M. Sawamura, *J. Am. Chem. Soc.*, 2008, **130**, 10044–10045; Au–Ag (d) Reference 2i; Cu (e) S. Perruchas, X. F. Le Goff, S. Maron, I. Maurin, F. Guillen, A. Garcia, T. Gacoin and J.-P. Boilot, *J. Am. Chem. Soc.*, 2010, **132**, 10967–10969.
- P. J. Wagner, G. S. Hammond, *Advances in Photochemistry*, Vol. 5, W. A. Noyes, Jr., G. S. Hammond and J. N. Pitts, Jr., eds., Interscience Publishers, New York, 1968, pp 21–156.
- (a) N. Komiya, M. Okada, K. Fukumoto, D. Jomori and T. Naota, *J. Am. Chem. Soc.* 2011, **133**, 6493–6496; (b) N. Komiya, M. Okada, K. Fukumoto, K. Kaneta, A. Yoshida and T. Naota, *Chem. Eur. J.* 2013, **19**, 4798–4811; (c) N. Komiya, N. Itami and T. Naota, *Chem. Eur. J.* 2013, **19**, 9497–9505.

- 6 (a) J. C. Ostrowski, M. R. Robinson, A. J. Heeger and G. C. Bazan, *Chem. Commun.* 2002, 784–785; (b) E. Q. Procopio, M. Mauro, M. Panigati, D. Donghi, P. Mercandelli, A. Sironi, G. D'Alfonso and L. De Cola, *J. Am. Chem. Soc.* 2010, **132**, 14397–14399; (c) A. Raimondi, M. Panigati, D. Maggioni, L. D'Alfonso, P. Mercandelli, P. Mussini and G. D'Alfonso, *Inorg. Chem.* 2012, **51**, 2966–2975; (d) V. A. Krylova, P. I. Djurovich, J. W. Aronson, R. Haiges, M. T. Whited and M. E. Thompson, *Organometallics* 2012, **31**, 7983–7993; (e) D. M. Zink, M. Bächle, T. Baumann, M. Nieger, M. Kühn, C. Wang, W. Klopfer, U. Monkowius, T. Hofbeck, H. Yersin and S. Bräse, *Inorg. Chem.* 2013, **52**, 2292–2305.
- 7 N. Komiya, T. Muraoka, M. Iida, M. Miyanaga, K. Takahashi and T. Naota, *J. Am. Chem. Soc.* 2011, **133**, 16054–16061.
- 8 C. A. Strassert, C.-H. Chien, M. D. Galvez Lopez, D. Kourkoulos, D. Hertel, K. Meerholz and L. De Cola, *Angew. Chem. Int. Ed.* 2011, **50**, 946–950.
- 9 Recent reports on H-X interactions in crystals: (a) R. H. Jones, K. S. Knight, W. G. Marshall, J. Clews, R. J. Darton, D. Pyatt, S. J. Coles and P. N. Horton, *CrystEngComm*, 2014, **16**, 237–243; (b) L. Barloy, E. Féghali, M. Henry, L. Karmazin-Brelot, C. Bailly and M. Pfeffer, *Organometallics*, 2013, **32**, 6195–6200; (c) C. Ma, J. Wang, L. Zhao, Y. Shi, W. Luo, Y. Yan, M. Fang, X. Wang and H.-K. Liu, *CrystEngComm*, 2013, **15**, 10311–10315; (d) M. Karanam and A. R. Choudhury, *Cryst. Growth Des.*, 2013, **13**, 4803–4814.
- 10 M. N. Burnett and C. K. Johnson, ORTEP-III: Oak Ridge Thermal Ellipsoid Plot Program for Crystal Structure Illustrations, Report ORNL-6895, Oak Ridge National Laboratory, Oak Ridge, 1996.
- 11 Y. Kawamura, H. Sasabe, and C. Adachi, *Jpn. J. Appl. Phys.* 2004, **43**, 7729–7730.
- 12 Red-shift in solid-state emission by  $\pi$ -stacking interactions: (a) M. Brinkmann, G. Gadret, M. Muccini, C. Taliani, N. Masciocchi and A. Sironi, *J. Am. Chem. Soc.*, 2000, **122**, 5147–5157; (b) K. Sokolowski, I. Justyniak, W. Śliwiński, K. Soltys, A. Tulewicz, A. Kornowicz, R. Moszyński, J. Lipkowski and J. Lewiński, *Chem. Eur. J.*, 2012, **18**, 5637–5645.
- 13 C. Postmus, Jr., I. A. Kaye, C. A. Craig and R. S. Matthews, *J. Org. Chem.* 1964, **29**, 2693–2698.
- 14 N. U. Hofsløkken and L. Skattebøl, *Acta Chem. Scand.* 1999, **53**, 258–262.
- 15 F. P. Fanizzi, F. P. Intini, L. Maresca and G. Natile, *J. Chem. Soc., Dalton Trans.* 1990, 199–202.
- 16 A. D. Becke, Modern Electronic Structure Theory, Part II, D. R. Yarkony, ed., World Scientific, Singapore, 1995.
- 17 Gaussian 09, Revision A.02, M. J. Frisch, G. W. Trucks, H. B. Schlegel, G. E. Scuseria, M. A. Robb, J. R. Cheeseman, G. Scalmani, V. Barone, B. Mennucci, G. A. Petersson, H. Nakatsuji, M. Caricato, X. Li, H. P. Hratchian, A. F. Izmaylov, J. Bloino, G. Zheng, J. L. Sonnenberg, M. Hada, M. Ehara, K. Toyota, R. Fukuda, J. Hasegawa, M. Ishida, T. Nakajima, Y. Honda, O. Kitao, H. Nakai, T. Vreven, J. A. Montgomery, Jr., J. E. Peralta, F. Ogliaro, M. Bearpark, J. J. Heyd, E. Brothers, K. N. Kudin, V. N. Staroverov, R. Kobayashi, J. Normand, K. Raghavachari, A. Rendell, J. C. Burant, S. S. Iyengar, J. Tomasi, M. Cossi, N. Rega, J. M. Millam, M. Klene, J. E. Knox, J. B. Cross, V. Bakken, C. Adamo, J. Jaramillo, R. Gomperts, R. E. Stratmann, O. Yazyev, A. J. Austin, R. Cammi, C. Pomelli, J. W. Ochterski, R. L. Martin, K. Morokuma, V. G. Zakrzewski, G. A. Voth, P. Salvador, J. J. Dannenberg, S. Dapprich, A. D. Daniels, Ö. Farkas, J. B. Foresman, J. V. Ortiz, J. Cioslowski and D. J. Fox, Gaussian, Inc., Wallingford CT, 2009.
- 18 (a) P. J. Hay and W. R. Wadt, *J. Chem. Phys.* 1985, **82**, 270–283; (b) P. J. Hay and W. R. Wadt, *J. Chem. Phys.* 1985, **82**, 299–310.
- 19 (a) M. M. Francl, W. J. Pietro, W. J. Hehre, J. S. Binkley, M. S. Gordon, D. J. DeFrees, and J. A. Pople, *J. Chem. Phys.* 1982, **77**, 3654–3665; (b) P. C. Hariharan and J. A. Pople, *Theor. Chim. Acta.* 1973, **28**, 213–222.
- 20 (a) M. E. Casida, C. Jamorski, K. C. Casida, and D. R. Salahub, *J. Chem. Phys.* 1998, **108**, 4439–4449; (b) R. E. Stratmann and G. E. Scuseria, *J. Chem. Phys.* 1998, **109**, 8218–8224.

## Table of contents entry

Chloro-substitution significantly increases the lower heat resistance of short-vaulted, non-substituted *trans*-bis(salicylaldiminato)Pt(II) complex crystals, and maintains the intense emission of long-vaulted analogues, which leads to intense solid-state emission of the vaulted crystals with low structural dependence.

